# Novel β-Amino Acid Derivatives as Inhibitors of Cathepsin A

Sven Ruf,[*,†] Christian Buning,[†] Herman Schreuder,[†] Georg Horstick,[†,§] Wolfgang Linz,[†] Thomas Olpp,[†] Josef Pernerstorfer,[†] Katrin Hiss,[†] Katja Kroll,[†] Aimo Kannt,[†] Markus Kohlmann,[†] Dominik Linz,[‡] Thomas Hübschle,[†] Hartmut Rütten,[†] Klaus Wirth,[†] Thorsten Schmidt,[†] and Thorsten Sadowski[†]

[†]Sanofi-Aventis Deutschland GmbH, Industriepark Höchst, 65926 Frankfurt, Germany
[‡]Universitätsklinikum des Saarlandes, Homburg/Saar, Germany

Ⓢ *Supporting Information*

**ABSTRACT:** Cathepsin A (CatA) is a serine carboxypeptidase distributed between lysosomes, cell membrane, and extracellular space. Several peptide hormones including bradykinin and angiotensin I have been described as substrates. Therefore, the inhibition of CatA has the potential for beneficial effects in cardiovascular diseases. Pharmacological inhibition of CatA by the natural product ebelactone B increased renal bradykinin levels and prevented the development of salt-induced hypertension. However, so far no small molecule inhibitors of CatA with oral bioavailability have been



described to allow further pharmacological profiling. In our work we identified novel β-amino acid derivatives as inhibitors of CatA after a HTS analysis based on a project adapted fragment approach. The new inhibitors showed beneficial ADME and pharmacokinetic profiles, and their binding modes were established by X-ray crystallography. Further investigations led to the identification of a hitherto unknown pathophysiological role of CatA in cardiac hypertrophy. One of our inhibitors is currently undergoing phase I clinical trials.
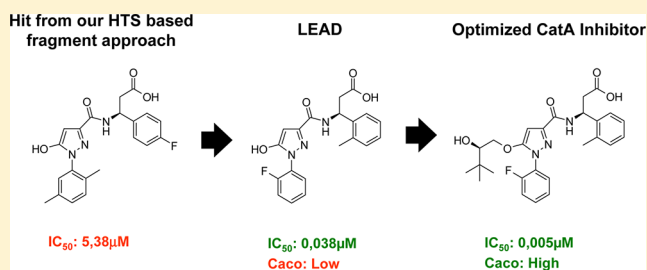
## INTRODUCTION

CatA is a lysosomal serine protease, which is also found in the extracellular space. The enzyme is a member of the α/β hydrolase fold family and shares structural homology with yeast carboxypeptidase Y.[1] Further research has established CatA as a multicatalytic enzyme with additional deamidase and esterase activities.[2] Distinct from the catalytic functions of CatA is its protective function in the lysosome: CatA stabilizes the high molecular weight enzyme complex made up of β-galactosidase and neuraminidase, and deficiencies of this complex lead to the severe human disease galactosialidosis.[3] A recent study in mice carrying a catalytically inactive CatA mutant demonstrated that CatA's protective function is distinct from its carboxypeptidase activity.[4]

Several peptide hormones have been described as substrates for CatA in vitro such as bradykinin, angiotensin I, and oxytocin.[5] Pharmacological inhibition of CatA by the natural product ebelactone B (Figure 1) increased renal bradykinin levels and prevented the development of salt-induced hyper-
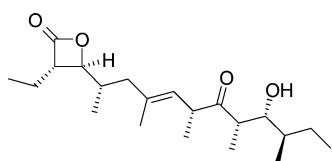
tension.[6] Similar effects were observed by antisense oligonucleotides suppressing the expression of CatA.[7] In addition to peptide hormones, the lysosomal receptor protein Lamp2a has also been identified as a substrate of this protease, linking CatA activity to autophagic processes.[8]

Since locally increased bradykinin levels have been reported to play a beneficial role in cardiac diseases,[9] we developed interest in the inhibition of CatA as a potential therapeutic intervention in this area. Contrary to established targets in the cardiac renin–angiotensin system such as ACE and NEP,[10] CatA is only weakly expressed in the vasculature and has an acidic pH optimum of activity. Both properties possibly exclude this enzyme from systemic peptide hormone turnover and suggest a role for CatA in the regulation of the local kallikrein–kinin and renin–angiotensin system.

In this article we describe the discovery of novel CatA inhibitors, which allowed us to identify a hitherto unknown pathophysiological role of this protease in cardiac hypertrophy and atrial arrhythmogenesis.

## CHEMISTRY

Our CatA inhibitors are easily recognized as products of amide coupling reactions starting from β-amino acids **4** and the pyrazole heterocycles **3** (Scheme 1).



**Figure 1.** Structure of ebelactone B.

**Scheme 1. General Synthetic Access to Cathepsin A Inhibitors 2 and 8[a]**
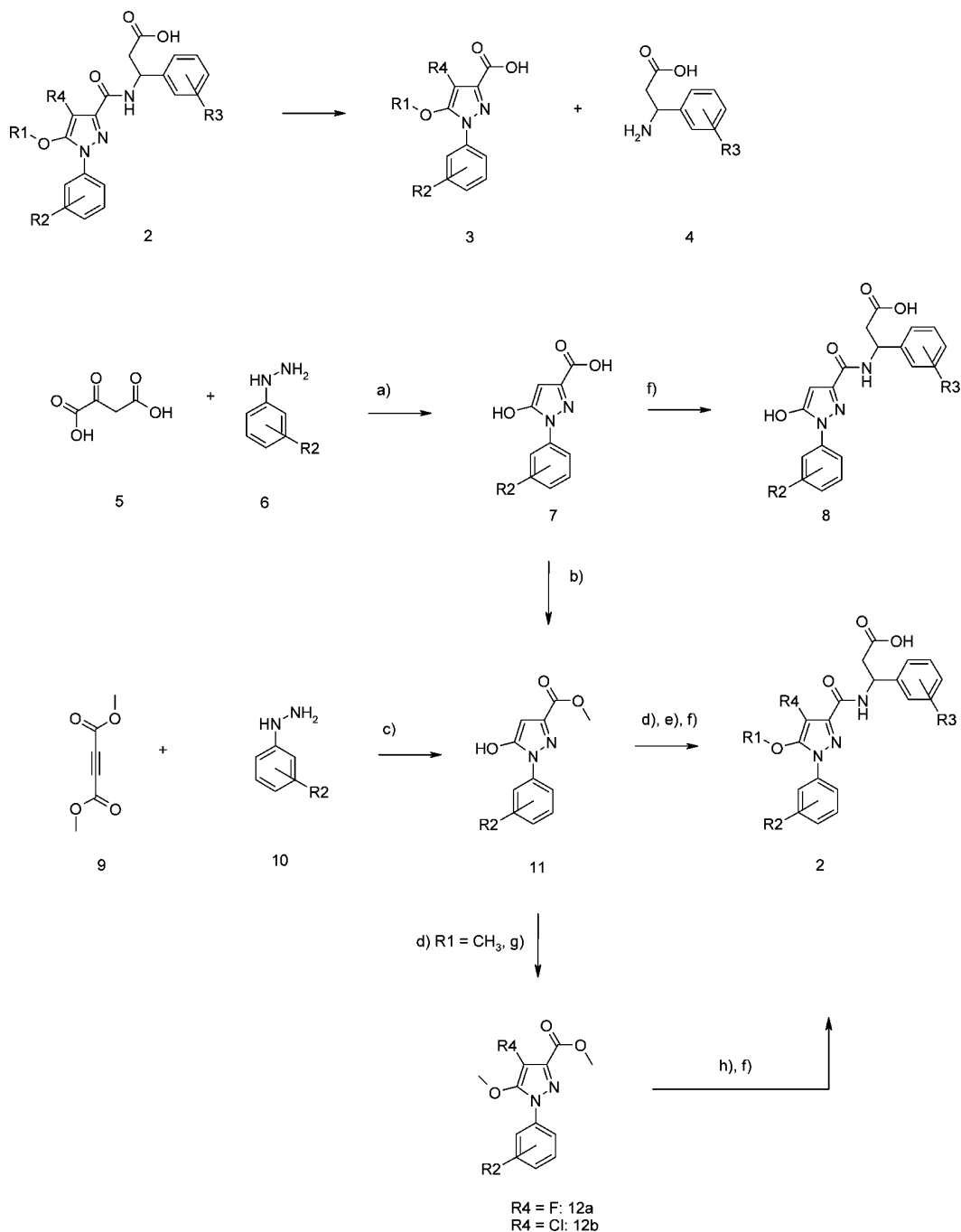


[a]Reagents and conditions: (a) $H_2SO_4$, rt, 4 h; (b) HCl, MeOH; (c) THF, NEt$_3$; (d) R$_1$X, (X = Br, Cl), Cs$_2$CO$_3$, THF; (e) NaOH, MeOH; (f) β-AS, TOTU, NEM, DMF, rt; (g) R4= Cl: SO$_2$Cl$_2$, HOAc, R4 = F: CH$_3$CN, Selectfluor, (h) LiOH, dioxane, water.

Synthetic pathways to β-amino acids have been reviewed elsewhere. A significant number of them are now commercially available.[11]

The pyrazole heterocycle **3** was accessible by addition of the corresponding hydrazine derivative **6** to oxalacetic acid **5** in diluted $H_2SO_4$. The condensation products **7** were easily isolated by filtration from the reaction mixture. An amide coupling of the intermediate **7** with β-amino acids using TOTU[12] as activating reagent delivered the inhibitors **8**.

In an alternative approach methyl esters **11** of the pyrazolonecarboxylic acids were synthesized by the addition of the corresponding hydrazines **10** to dimethyl acetylenedicarbox-

ylate **9**. Further functionalization of the hydroxy group was then accomplished by alkylation of the methyl esters **11** with alkyl halogenides in acetone with $Cs_2CO_3$ as base. Under these reaction conditions a selective O-alkylation of the pyrazolone precursors **11** was observed.

Introduction of a halogen in the 4-position of the pyrazolone core was accomplished with sulforyl chloride or Selectfluor applied on the 5-methoxy-1-(2-fluorophenyl)pyrazol-3-carboxylic acid methyl ester.

Introduction of a hydroxyl group in the 5-alkoxy-substituent resulted from the reduction of **13** with $NaBH_4$ in methanol (Scheme 2). **13** was synthesized according to Scheme 1 with

**Scheme 2. Synthesis of Cathepsin A Inhibitors 13−16[a]**
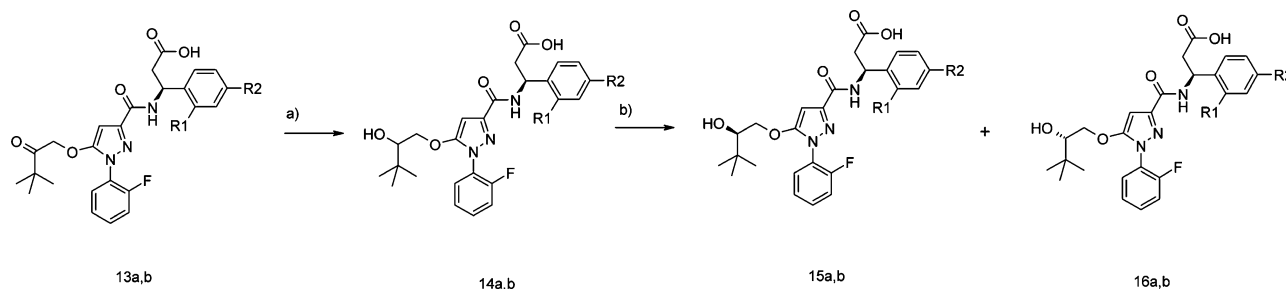


[a]**13−16a**: R1 = CH₃, R2 = H. **13−16b**: R1 = R2 = Cl. Reagents and conditions: (a) NaBH₄, MeOH; (b) chiral chromatography.
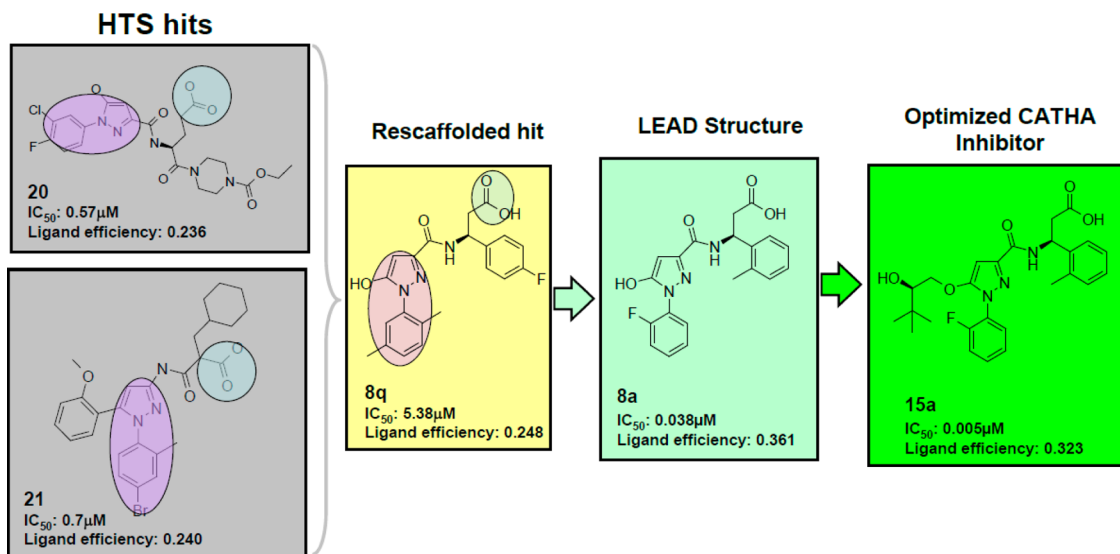


**Figure 2.** Identification of preferred chemical motifs (virtual fragments) from HTS hits (blue and purple circles) and subsequent combinations by H2L chemistry.

bromopinacolone used as alkyl bromide. The mixture of diastereomers **14** obtained after reduction was separated by chiral chromatography, yielding pure stereoisomers **15** and **16**. The configuration of the chiral alcohol carbon atom was arbitrarily assigned *R* to the isomer with the shortest retention time on the chiral column.

The ¹H NMR spectra of **15/16a** and of **15/16b** were very similar. However, these compounds could be clearly distinguished by their different retention times on an LCMS system with an elongated gradient method on an achiral column.

### ■ IDENTIFICATION OF THE LEAD STRUCTURE 8A

With no small molecule inhibitors of CatA besides ebelactone B described in the literature we initiated a HTS of our compound collection, which was successful in identifying several hit series with high activity (<0.5 μM) on CatA confirming the druggability of CatA with small molecules. Unfortunately the most active hits series from the HTS turned out to be of only limited use for the following reasons: (A) toxicological issues of hits known from other projects; (B) observed proteolytic cleavage during crystallization; (C) high MW combined with high lipophilicity and low ligand efficiency (not leadlike).[13]

Therefore, on the basis of our HTS results, we initiated explorative hit to lead chemistry in order to identify a suitable lead structure. Working in this early phase without reliable SAR patterns, we were looking for guiding principles to direct our chemical activities. By detailed analysis of the HTS hit structures,

we identified certain chemical subunits present in several hit clusters. Chemical building blocks were selected with high similarity to the virtual fragments for suitable combinations by parallel chemistry.

The chosen procedure and project progression is shown in Figure 2. The hit compounds **20** and **21** revealed that aliphatic chains with a carboxylic acid terminus and the pyrazole scaffold were preferred chemical motifs for CatA inhibitors. A first series of parallel syntheses led to the identification of the rescaffolded hit **8q**, which had lost activity by a factor of 10 compared to the starting point **20**, but because of the reduced molecular weight, the ligand efficiency was in the same range. From a chemical perspective **8q** was a very attractive starting point for us. We initiated X-ray crystallographic studies in order to obtain information of the binding mode of **8q** and started parallel synthesis activities focusing on variations of the phenyl residues in the β-amino acid and pyrazole parts of the molecule.

By starting from **8q** and applying the strategy described above, we were able to increase the activity by a factor of 100 and to identify (*S*)-β-amino acids as the preferred enantiomeric form for the construction of CatA inhibitors (see derivatives **8s** and **8t** in Table 1).

As can be seen from Table 1, the highest inhibitory activity in this series was observed with **8b** featuring a biphenyl substituent in the β-amino acid residue.

The introduction of an oxygen linker between the two phenyl groups (**8j**) led to somewhat reduced inhibitory activity. By a

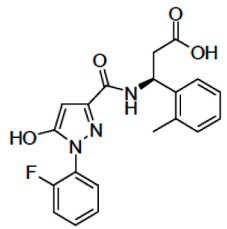## Table 1. Biological Data of Compounds 2, 8, 13,15, 16
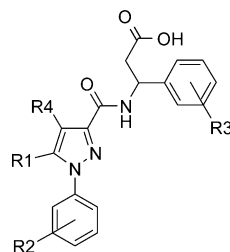


| compd | R1 | R2 | R3 | R4 | configuration of $\beta$-amino acid | IC$_{50}$ ($\mu$M) |
|---|---|---|---|---|---|---|
| **2a** | -OCH$_3$ | 2-F | 2-Me | H | S | 0.026 |
| **2b** | -OC$_2$H$_5$ | 2-F | 2-Me | H | S | 0.015 |
| **2c** | -OCH$_2$CH(CH$_2$)$_2$ | 2-F | 2-Me | H | S | 0.015 |
| **2d** | -OCH$_3$ | 2-F | 2-Me | F | S | 0.03 |
| **2e** | -OCH$_3$ | 2-F | 2-Me | Cl | S | 0.110 |
| **2f** | H | H | 2-Me | -OH | S | 0.110 |
| **2g** | H | H | 2-Me | -OMe | S | 0.100 |
| **8a** | OH | 2-F | 2-Me | H | S | 0.038 |
| **8b** | OH | 2-F | 4-(4-F-phenyl) | H | racemate | 0.025 |
| **8c** | OH | 2-Cl | 2-Me | H | S | 0.057 |
| **8d** | OH | 3-F | 2-Me | H | S | 0.059 |
| **8e** | OH | 2-F | 2-methyl-5-fluoro | H | racemate | 0.076 |
| **8f** | OH | H | 2,3-dichloro | H | racemate | 0.100 |
| **8g** | OH | 4-F | 2-methyl | H | S | 0.087 |
| **8h** | OH | 2,4-difluoro | 2,3-dichloro | H | racemate | 0.120 |
| **8i** | OH | 3-Cl | 2-methyl | H | S | 0.102 |
| **8j** | OH | H | 4-phenoxy | H | racemate | 0.200 |
| **8k** | OH | 2-F | H | H | racemate | 0.226 |
| **8l** | OH | 2-F | 3-Me | H | S | 0.252 |
| **8m** | OH | 2-F | 4-Me | H | S | 0.274 |
| **8n** | OH | 2-F | 2-OMe | H | S | 0.357 |
| **8o** | OH | 2-F | 2-CF$_3$ | H | S | 0.375 |
| **8p** | OH | 2,5-dimethyl | 4-phenyl | H | racemate | 0.803 |
| **8q** | OH | 2,5-dimethyl | 4-F | H | racemate | 5.38 |
| **8r** | OH | 4-Cl | 2,5-dichloro | H | racemate | >30 |
| **8s** | OH | H | 2-Me | H | S | 0.070 |
| **8t** | OH | H | 2-Me | H | R | 7.8 |
| **13a** | (R)-OCH$_2$-C(O)$^t$Bu | 2-F | 2-Me | H | S | 0.003 |
| **13b** | (R)-OCH$_2$-C(O)$^t$Bu | 2-F | 2,4-dichloro | H | S | 0.06 |
| **15a** | (R)-OCH$_2$-CH(OH)$^t$Bu | 2-F | 2-Me | H | S | 0.005 |
| **15b** | (R)-OCH$_2$-CH(OH)$^t$Bu | 2-F | 2,4-dichloro | H | S | 0.050 |
| **16a** | (S)-OCH$_2$-CH(OH)$^t$Bu | 2-F | 2-Me | H | S | 0.01 |
| **16b** | (S)-OCH$_2$-CH(OH)$^t$Bu | 2-F | 2,4-dichloro | H | S | 0.07 |

switch to simple phenyl residues on the $\beta$-amino acid scaffold, the ortho-tolyl derivative **8a** showed a dramatic improvement in inhibitory activity compared to the unsubstituted one **8k**. Putting the methyl group in meta or para position resulted in a drastic reduction in activity as seen with examples **8l,m**. The same observation was made after replacement of the ortho methyl group by sterically more demanding or polar groups, e.g., in **8n** or **8o**. Also an introduction of additional substituents did not lead to an affinity improvement as demonstrated by **8e,g,h**. Looking at the phenyl residue bound to the pyrazole heterocyclic core, we determined that the ortho-fluoro derivative **8a** was the most promising. It was slightly more active than the ortho-chloro and meta-fluoro analogues **8c** and **8d** and also more active than the unsubstituted derivative **8s**. In good agreement with this observation is the further decreased biological activity of the *m*-Cl derivative **8i** or the *p*-F derivative **8g**. As observed in the phenyl residue on the $\beta$-amino acid, the introduction of a second

substituent on this *N*-phenyl ring of the pyrazol was not beneficial in terms of activity. That was especially the case for two substituents in the 2- and 5- position of the phenyl ring, as can be seen in **8p** and **8q**. On the basis of these data, we chose **8a** for a full lead profile, and our obtained data are presented in Table 2. Typical for this series of compounds was the low metabolic lability in human microsomes and the absence of CYP3A4 inhibition. We observed no undesired activities on the human hERG channel and no hints for genotoxicity in the micronucleus and for mutagenicity in the AMES II test system. In addition, this compound had low log $D$ and PSA values and a high solubility. The downside of this compound, however, was the limited cell permeability as measured in the CACO-2[14] assay. Regarding selectivity, **8a** showed submicromolar activity on neutral endopeptidase (NEP).

**Table 2. ADME and Safety Data of Lead 8a**

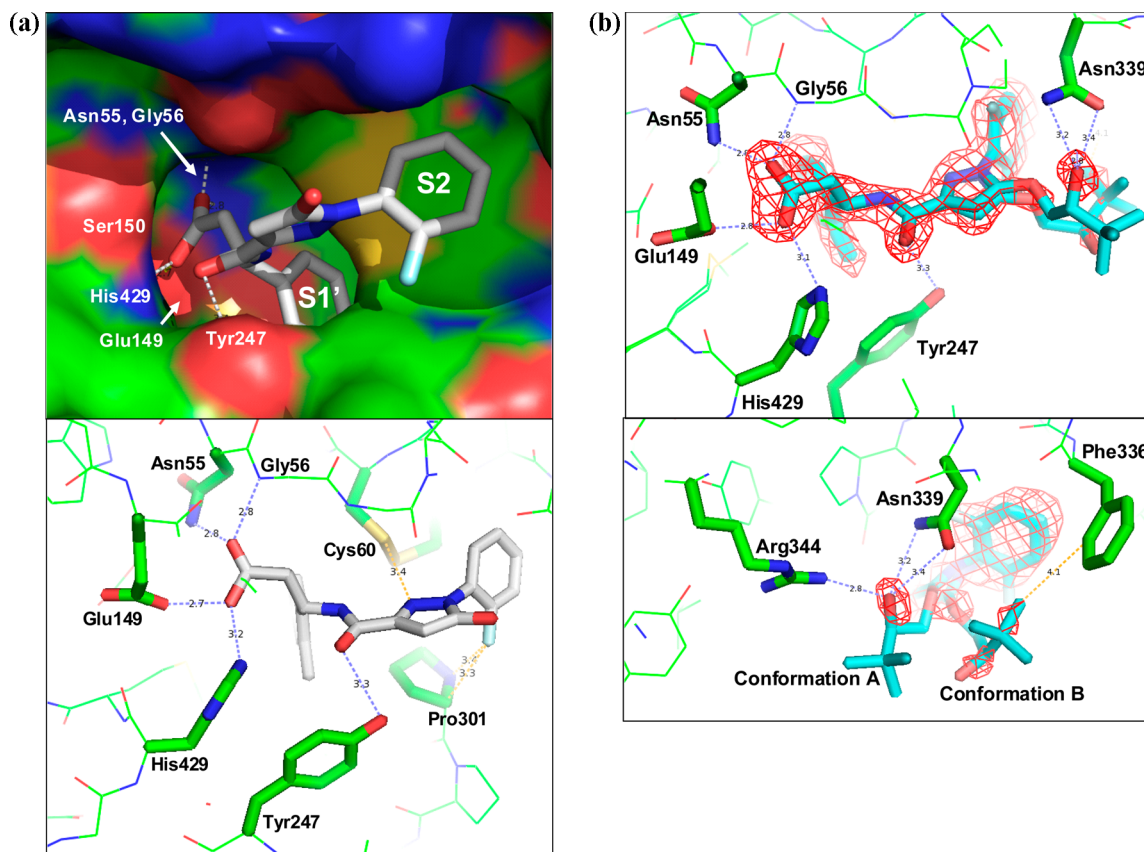| | |
|---|---|
| | **8a** |
| CatA IC$_{50}$ | 0.038 |
| Solubility [mg/ml] / log D | >0.18 / -0.16 |
| Rule of 5 / PSA [A²]/ Ligand efficiency [kcal/mol] | OK / 104.5 / 0.361 |
| Microsomal lability (human / rat) | Low (10/10)% |
| CYP3A4 inhibition | >30µM |
| Caco-2 [x10$^{-7}$ cm/sec] | Low (0,5) |
| hERG | >10 µM |
| AMES / MNT | All negative |



**Figure 3.** (a) X-ray structure of lead **8a** showing important hydrogen bonding interactions with the CatA enzyme. The top panel shows the solvent accessible surface of CatA, while the lower panel shows the atomic model. (b) Two views of the $F_o - F_c$ omit map of **15a** in CatA as well as the atomic model. The contour level is $3\sigma$. Superimposed are the two conformations of **15a** we fitted (see text).

## CRYSTAL STRUCTURES OF 8A AND 15A BOUND TO CATA[15]

The crystal structure of the CatA precursor (known as human protective protein precursor) was solved by Rudenko et al. in 1995.[16,17] This precursor consists of a single chain of 542 amino acids. However, the precursor is inactive because the active site is blocked by the excision peptide. To obtain the active form of the enzyme, the 54 kDa CatA precursor was proteolytically transformed into the active mature form by cleavage of a 2 kDa excision peptide with trypsin-Sepharose followed by gel filtration. The activated protein was crystallized, and the initial structure was solved using the structure of the precursor as a search model. Details of the active crystal structure will be published elsewhere. The mature enzyme consists of two polypeptides, which are linked together by disulfide bonds to form a monomer. The catalytic triad of cathepsin A is located in the 32 kDa chain and consists of the amino acids Ser150, His429, and Asp372.

The crystal structure of **8a** in complex with the CatA protein was solved at a resolution of 2.17 Å (Figure 3a, compound−protein interactions listed in Table 3) and is the first published

**Table 3. Interactions between 8a and Cathepsin A**

| atom 1 | atom 2 | distance (Å) | type |
|---|---|---|---|
| F28 | N Pro301 | 3.4 | van der Waals |
| | CA Pro301 | 3.3 | van der Waals |
| N2 | SG Cys60 | 3.4 | van der Waals |
| O15 | OH Tyr247 | 3.3 | H bond |
| O26 | OE2 Glu149 | 2.7 | H bond[a] |
| | NE2 His429 | 3.2 | ionic[a] |
| O27 | ND2 Asn55 | 2.8 | H bond |
| | N Gly56 | 2.8 | H bond |

[a]Depending on the protonation state of the residues involved.

structure of the active CatA enzyme with a small molecule ligand. The carboxylate group of **8a** is accommodated in the carboxylate recognition site making hydrogen bonds with the OE2 of Glu149, the NE2 of His429, the NH2 of Asn55, and the main-chain N of Gly56. The ortho-methylbenzene substituent in the β-amino acid part of the inhibitor is located in the S1′ pocket. This S1′ pocket is part of a deep lipophilic tunnel within the enzyme. Finally, the carbonyl oxygen of the central amide group makes a hydrogen bond with the OH of Tyr247 and the hydroxy group in the 5-position of the pyrazole ring points toward the solvent and does not interact with the protein.

The crystal structure of **15a** in complex with the CatA protein was solved at a resolution of 2.04 Å (Figure 3b, compound−protein interactions listed in Table 4).

The binding mode of the common core of **15a** and **8a** is analogous. The 3,3-dimethylbutane-2-ol substituent has weak electron density and is very likely disordered.

We modeled two orientations: one with the OH group interacting with the side chains of Asn339 and Arg344 and one where this group faces the solvent. In the latter case the tertiary butyl group has the potential to undergo van der Waals interactions with the side chain of Phe336. Also the ortho-fluorobenzene group is present in two orientations: one orientation where the fluoro group interacts with the main-chain O of Pro59 and the OD1 of Asp339 and one orientation where this fluoro group faces the solvent.

From these crystal structures, it is not immediately clear why **15a** is much more potent than **8a** (IC$_{50}$ of 5 nM vs 38 nM).

**Table 4. Interactions between 15a and Cathepsin A**

| atom 1 | atom 2 | distance (Å) | type |
|---|---|---|---|
| F7A[a] | CA Pro301 | 3.4 | van der Waals |
| F7B[a] | O Pro58 | 2.7 | van der Waals |
| | ND2 Asn339 | 2.7 | van der Waals |
| N9A/B | SG Cys60 | 3.4/3.3 | van der Waals |
| C11A | O Gly57 | 3.1 | van der Waals |
| C12A | O Gly57 | 3.5 | van der Waals |
| O13A | ND2 Asn339 | 3.4 | H bond |
| O16A | OD1 Asn339 | 3.4 | H bond |
| | ND2 Asn339 | 3.2 | H bond |
| | NH2 Arg334 | 2.8 | H bond |
| O22A/B | OH Tyr247 | 3.3/3.4 | H bond |
| C26A/B | OE2 Glu149 | 3.4/3.5 | van der Waals |
| O27A/B | ND2 Asn55 | 2.8/2.8 | H bond |
| | N Gly56 | 2.8/2.8 | H bond |
| O28A/B | OE2 Glu149 | 2.8/2.9 | H bond[b] |
| | NE2 His429 | 3.2/3.1 | ionic[b] |
| C30A | CE Met430 | 3.4 | van der Waals |
| C31A/B | CE Met430 | 3.2/3.5 | van der Waals |
| C32A | OD1 Asp64 | 3.3 | van der Waals |

[a]The inhibitor has been fitted in two conformations: A and B.
[b]Depending on the protonation state of the residues involved.

However, if we look at Figure 3b, lower panel, we see in conformation A the hydroxyl making decent hydrogen bonds with the side chains of Asn339 and Arg344 whereas in conformation B the lipopilic part of the 3,3-dimethylbutane-2-ol substituent makes van der Waals interactions with the side chain of Phe336. The increased potency of **2c** (IC$_{50}$ = 15 nM) with a lipophilic cyclopropylmethoxy residue in the 5-position of the pyrazole gives an additional confirmation for the beneficial influence of van der Waals interactions in this region of the enzyme on ligand activity. In the case of **15a** we therefore assume that both interactions identified above will contribute positively to the binding affinity. These observed binding interactions have the additional advantage that the loss of entropy typically accompanied upon ligand binding is reduced because the fixation of the flexible 3,3-dimethylbutane-2-ol-side chain of **15a** to a single conformation is avoided. The overall result from these combination of ligand binding descriptors is the observed significantly stronger binding.

## LEAD OPTIMIZATION

The lead compound **8a** already has a remarkably clean overall in vitro ADME and safety profile (see Table 2). However an obvious parameter for improvement is the low cell permeability of **8a**, which results in a low oral bioavailability of below <5%. We also aimed for a further improvement of the target affinity.

Our strategies to overcome the low cell permeability of our lead **8a** targeted the low log D of −0.16. From a chemical point of view the free carboxylate group and the pyrazolone core are ideal starting points for the introduction of lipophilicity by suitable structural modifications.

A classical approach to overcome low permeability in the case of aliphatic carboxylic acids is to use prodrugs.[18] The conversion of the acid into an ester drastically reduces the polarity and in many cases allows the compound to cross cellular membranes. In the case of **8a** the use of an ester prodrug would result in the formation of a CatA inhibitor with low cell permeability in the plasma. However, the CatA expression in the systemic circulation is rather low and the low cell permeability of the
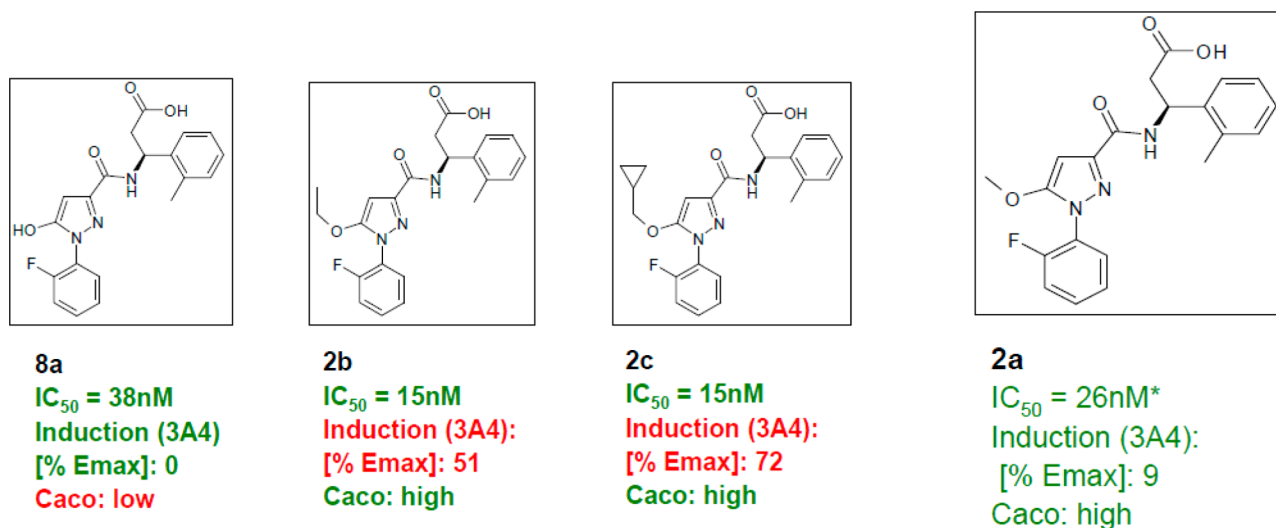
**8a**
IC$_{50}$ = 38nM
Induction (3A4)
[% Emax]: 0
Caco: low

**2b**
IC$_{50}$ = 15nM
Induction (3A4):
[% Emax]: 51
Caco: high

**2c**
IC$_{50}$ = 15nM
Induction (3A4):
[% Emax]: 72
Caco: high

**2a**
IC$_{50}$ = 26nM*
Induction (3A4):
[% Emax]: 9
Caco: high

**Figure 4.** Dependency of cell permeability (Caco) and CYP3A4 induction on 5-substituents on the pyrazole heterocycle. Green values are favorable, and red values are disfavorable.

metabolized prodrug could prevent our inhibitor from entering targeted tissues with a significant CatA expression. For these reasons we saw a serious risk that the use of ester prodrugs would limit our pharmacological evaluation of this novel target and discarded this approach.

We therefore focused our investigations on the 4- and 5-position of the pyrazolone for the introduction of structural modifications. First, we introduced lipophilic extensions at the oxygen in the 5-position. Figure 5 indicates the general trends we observed regarding target affinity and permeability. Both permeability and target affinity improve when substituting the pyrazolone with either ethyl or methylcyclopropyl, resulting in perfectly permeable and highly active compounds. Compounds **2b,c** have an IC$_{50}$ of 15 nM combined with a high Caco classification as an indicator for good cell permeability. However, the improvement in biological activity and cell permeability was correlated with induction of CYP3A4, a strong indicator of potential later issues with drug−drug interactions as demonstrated with derivatives (**2b,c**) (see Figure 4).

Since the lead compound does not show any CYP3A4 induction, we concluded that the introduced lipophilicity in the 5-position of the pyrazolone had to be counterbalanced with some polarity in this part of the molecule.

Given the X-ray structural information of the lead compound **8a**, we extensively used structure-based design technologies to identify the most promising polar substituent in the 5-position of the pyrazolone. Initially, we analyzed the CatA binding pocket in detail using the knowledge-based approach Superstar.[19] Superstar proposes hot spots for the placement of chemical functionalities in the active site based on a thorough statistical analysis of published X-ray data. We used the alcohol −OH and the methyl probe to identify promising regions for additional polarity combined with a lipophilic linker (see Figure 5a). The regions as detected by SuperStar correspond to a moderately increased probability of binding of either lipophilic or alcoholic groups as indicated by the propensity level. From this analysis we concluded that the extension of the pyrazolone oxygen by a lipophilic linker is favored including a terminal hydroxyl group addressing hydrogen bonding interactions to ASN339 and/or ARG344. Extensive docking studies have been performed using

the GLIDE docking software to design a suitable lipophilic linker[20] (see Figure 5b).

Consequently, we synthesized and tested alkyl chains having either hydroxyl group or alternatively a carbonyl functional group to form hydrogen bonds with the proposed amino acids. By doing so, we identified the two compound pairs **13a,b** and **15a,b**. Both pairs of compounds have cell permeabilities of >20 × 10$^{-7}$ cm/s, and derivatives with R$_3$ = Me (see Table 1) have a significantly improved affinity compared to the initial lead compound **8a**. As important has been the observation that both **15a,b** show no significant CYP3A4 induction.

As predicted by our rational design approach, **13a** and **15a** show the highest in vitro biological activity on CatA measured in our series. **13b** and **15b** with a less preferred phenyl substitution pattern in the β-amino acid part of the molecule are comparable to **2a** regarding the biological activity.

Interestingly, the configuration on the chiral alcohol carbon atom has only a minor influence on the in vitro CatA activity, with the stereoisomer **16** having lost approximately a factor of 2 compared to **15**.

In addressing the 4-position of the pyrazolone core, we investigated halogen and oxygen substituents. While fluorine was well tolerated in terms of activity (**2d**), compounds with chlorine (**2e**), hydroxyl (**2f**), and methoxy substituent (**2g**) lost activity by a factor of 3 compared to **2a** (Table 1).

Our novel CatA inhibitors **2a**, **15a**, **15b** show high selectivity toward other targets. From an array of 10 proteases tested we only found micromolar activity on NEP for **2a**, which was no longer present in **15a** or **15b**. As shown in Figure 6 the NEP activity in our lead series is limited to a small substructural class featuring a free hydroxyl group on the pyrazole core in combination with chlorinated β-phenylalanine residues. In general the introduction of alkoxy residues into the 5-position of the pyrazole resulted in IC$_{50}$(NEP) > 1 μM.

Compounds **2a**, **15a**, and **15b** represent promising combinations of high cell permeability and acceptable CYP3A4 induction profile. We also found no hints for CYP inhibition or hERG channel interactions, and the compounds were clean in AMES and MNT testing. A broad study of **2a** and **15a** on the commercial CEREP profile[21] of a diverse set of 100 ion channels,
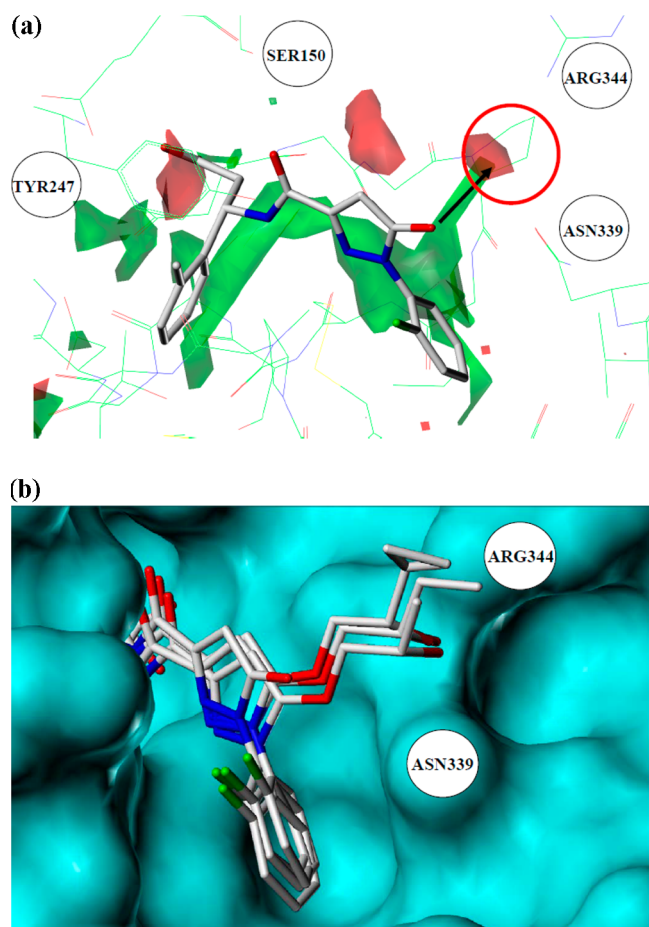
**Figure 5.** (a) Superstar propensity plot of cathepsin A binding pocket and compound **8a** as determined by X-ray analysis (red, OH probe, propensity level 1.8; green, methyl probe, propensity level 1.6). Atom colors for compound **8a** are as follows: carbon, gray,; oxygen, red; nitrogen, blue; fluorine, green. Atom colors for CatA binding site are as follows: carbon, green; oxygen, red; nitrogen, blue; sulfur, yellow. The black arrow is the extension vector that is directed to the preferred area for a hydroxyl group marked by the red circle originating from the oxygen in the 5-position of the pyrazolone. Additionally, positions of relevant amino acids are indicated. (b) Cathepsin A binding pocket including compound **8a** and docking poses from the structure-based design cycle. Atom colors are as follows: carbon, gray; oxygen, red; nitrogen, blue; fluorine, green. In cyan the solvent accessible surface of the binding site is shown.

enzymes, and receptors revealed no hits above 70% inhibition at 10 $\mu$M.

For a further differentiation between the compounds **2a**, **15a**, and **15b** we initiated pharmacokinetic studies in rat, and the results are presented in Table 5. $C_{max}$ and AUC values of **2a** in

**Table 5. Pharmacokinetic Data after po Administration of 10 mg/kg 2a, 15a,b in 25% Glycofurol/Cremophor (75/25) Solution to Male Sprague Dawley Rats**

|  | 2a | | 15a | | 15b | |
|---|---|---|---|---|---|---|
|  | plasma | heart | plasma | heart | plasma | heart |
| $C_{max}$ (ng/mL) | 22200 | 3720 | 1360 | 426 | 2670 | 872 |
| $AUC_{(0-inf)}$ (ng·h/mL) | 130000 | 16000 | 5300 | 1600 | 9300 | 2600 |

the plasma are considerably higher compared to those of **15a** and **15b**. In addition the overall tissue distribution profile is similar in all three compounds with the highest tissue exposure in the heart observed with **2a**.

## ■ BIOLOGICAL ACTIVITY: IN VIVO/PHARMACOLOGICAL RESULTS

To test whether CatA inhibition would increase urinary bradykinin, we collected urine from rats over a 6 h period before and after treatment with compounds **2a**, **15a**, **15b** at 30 mg/kg po. Bradykinin was then determined by a specific RIA.

Figure 7a shows that although basal urinary bradykinin levels varied between the three treatment groups, all compounds increased the amount of bradykinin by 2- to nearly 3-fold. This effect seemed not to be mediated by compound-induced alterations of glomerular filtration rate, as creatinine excretion was not changed by compound treatment (data not shown). In our opinion different excretion rates of parent compound into the distal tubule of the kidney might explain the observed differences in diuretic activity.

Bradykinin is known for its diuretic effects, which are mediated by increased renal blood flow and inhibition of sodium reabsorption in the collecting duct.[22] To determine whether the increased amount of urinary bradykinin observed under CatA inhibition translated into enhanced diuresis, anesthetized rats received bolus injection of compounds **2a**, **15a**, **15b** at 1 mg/kg iv and urine was collected through cannulas inserted into the ureters in five succeeding time periods of 20 min. Albumin in physiological saline was infused throughout the experimental period to ensure urine flow. In vehicle-treated
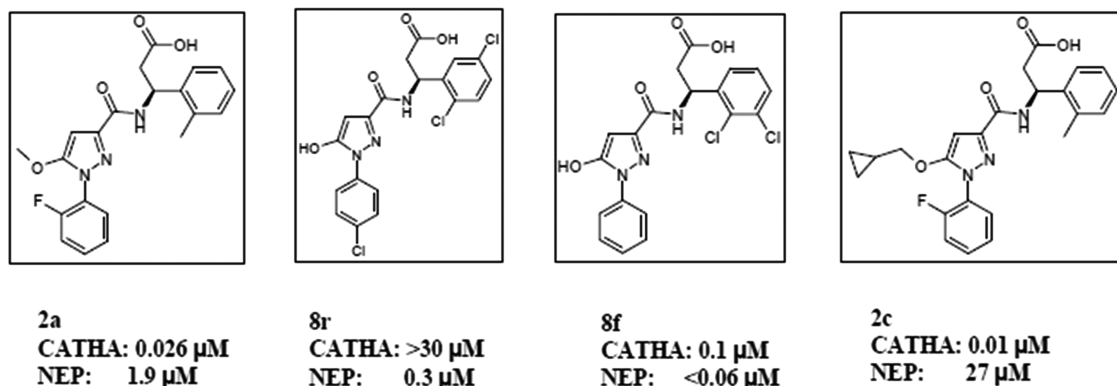


**2a**
CATHA: 0.026 $\mu$M
NEP:   1.9 $\mu$M

**8r**
CATHA: >30 $\mu$M
NEP:   0.3 $\mu$M

**8f**
CATHA: 0.1 $\mu$M
NEP:   <0.06 $\mu$M

**2c**
CATHA: 0.01 $\mu$M
NEP:   27 $\mu$M

**Figure 6.** IC$_{50}$ on CatA and NEP of several compounds from our lead series.
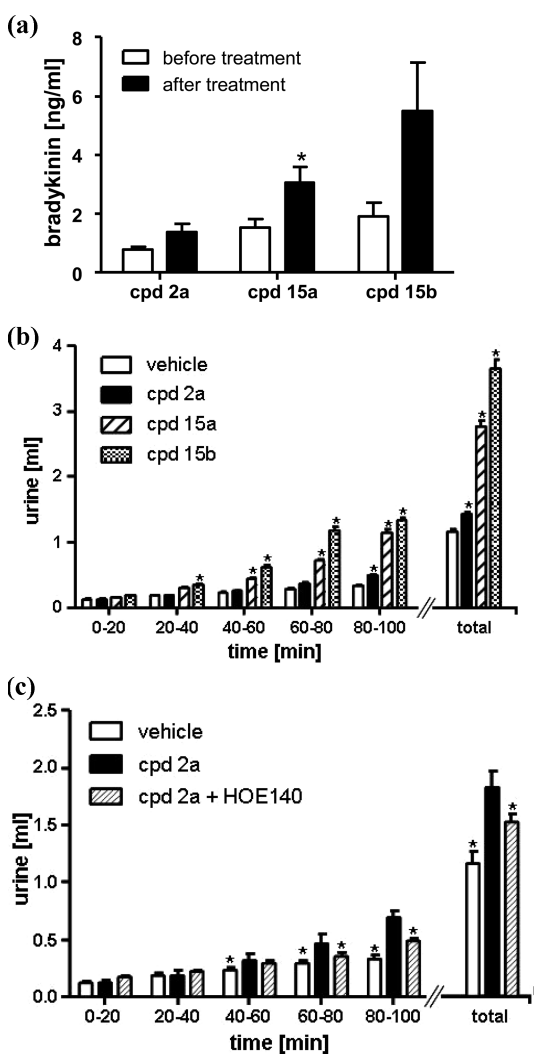
**Figure 7.** CatA inhibition leads to bradykinin-dependent diuresis in rats. (a) Compounds **2a**, **15a**, and **15b** increased urinary bradykinin levels compared to untreated rats. Data are expressed as the mean ± SEM ($n$ = 9−10). Statistical analysis was done by paired $t$ test. (b) Anesthetized rats received iv bolus injections of compounds **2a**, **15a**, and **15b**. Urine was collected for the given intervals from cannulated ureters and quantified. Data are expressed as the mean ± SEM ($n$ = 5−7). Statistical analysis was done by two-way ANOVA with Bonferroni post-tests relative to vehicle. (c) Compound **2a** was given iv at 10 mg/kg in the presence of HOE140 given at 0.5 mg/kg iv. Urine samples were collected as described in (b). Statistical analysis was done by two-way ANOVA with Bonferroni post-tests relative to compound x: (∗) significance was set to $p < 0.05$.

animals the urine volume increased only slightly over time. In contrast, all compounds significantly increased urine flow over time (**2a**, 14.3 $\mu$L/min; **15a**, 27.7 $\mu$L/min; **15b**, 36.5 $\mu$L/min; vs vehicle, 11.6 $\mu$L/min, $p < 0.001$). The magnitude of these effects correlated well with the compounds' ability to increase urinary bradykinin levels (Figure 7b). Finally, the diuretic activity induced by 10 mg/kg **2a** could be significantly attenuated by the simultaneous application of the bradykinin receptor antagonist HOE140 (15.3 $\mu$L/min vs 18.3 $\mu$L/min, $p < 0.001$), demonstrating the kinin dependency of this effect (Figure 7c).

Besides its renal effects, bradykinin has been shown to play an important role in reducing the development of cardiac hypertrophy.[23] Moreover, expression of CatA has been

demonstrated in cardiac tissue[24] and could be involved in the local degradation of bradykinin. We speculated that CatA inhibition could therefore be protective in cardiac hypertrophy. Compound **2a** was chosen because of its favorable ADME profile that makes it especially suitable for chronic in vivo testing. The heart failure animal model used in this study makes use of a continuous angiotensin II (Ang II) infusion in male hypercholesteremic ApoE ko mouse. This animal model combines the two well-known cardiovascular risk factors hypercholesterolemia and hypertension to experimentally establish cardiac hypertrophy and heart failure in a short period of time. Compound **2a** was administered at 100 mg kg$^{-1}$ day$^{-1}$ po and compared to the aldosterone antagonist spironolactone (100 mg kg$^{-1}$ day$^{-1}$ b.i.d.). The results are summarized in Table 6.

To judge cardiac hypertrophy parameters, biometric weight data were collected 4 weeks after compound treatment at the study end. While there was no difference in the overall body weights between the tested groups, clear and significant differences in the left ventricular wet weight and the left ventricular wet weight to body weight (LV wwt/BW) ratios were found. Treatment with compound **2a** significantly reduced the Ang II induced increase of both LV wwt ($p = 0.001$) and LV wwt/BW ratio ($p = 0.0038$) almost to control levels.

In line with the improvement of left ventricular hypertrophy parameters the functional hemodynamic pressure−volume (p−v) loop characterization revealed additional beneficial effects of CatA inhibition in this heart failure mouse model. As first functional parameters we measured mean arterial pressure (MAP) and heart rate (HR) within the ascending aortic arch. This was done just before the tip catheter was finally inserted into the left ventricle for p−v loop analysis. While there existed a clear and significant elevation of MAP in the Ang II infused placebo group compared to the NaCl control group ($p = 0.0299$), compound **2a** did not induce any significant changes in MAP and HR under Ang II stimulated conditions. In contrast, compound **2a** led to a significant improvement of left ventricular end diastolic pressure ($p = 0.0012$) and the left ventricular relaxation time $\tau$ (Weiss) ($\tau_w$, $p = 0.0014$) when compared to the Ang II placebo group. No significant changes, however, could be determined in the ejection fraction between all groups. And the Ang II induced elevation in left ventricular end-systolic pressure (LVESP) was not corrected by compound **2a** treatment. Overall, inhibition of CatA was not inferior to treatment with the marketed aldosterone antagonist spironolactone.

Additionally, CatA expression has been shown to be increased in human cardiac atrial tissue.[21] To investigate the effect of CatA inhibition by compound **2a** on the development of an atrial substrate for atrial fibrillation (AF), we used male Wistar rats with ventricular ischemia/reperfusion (I/R), a rat model for atrial structural remodeling. Three months after surgery the median duration of atrial fibrillation induced by burst pacing, a functional parameter describing the progression of an arrhythmogenic substrate in the atrium, was decreased in **2a** treated I/R rats in comparison to placebo treated I/R rats (0.69 ± 3.08 s vs 25.00 ± 18.09 s, $p < 0.01$) (Figure 8). This indicates that **2a** displays potent atrial antiarrhythmic effects in a rat model for atrial structural remodeling which leads to less stable AF episodes and attenuates the progression of AF.

## ■ CONCLUSION

The identification of novel small molecule inhibitors of cathepsin A is reported for the first time. By employing a fragment approach on HTS results, we rapidly identified **8a** as a

**Table 6. Effects of Compound 2a and Spironolactone in a Mouse Model of Ang II Induced Cardiac Hypertrophy[a]**

| | NaCl + placebo (N = 10) | Ang II + placebo (N = 13) | Ang II + **2a** (N = 14) | Ang II + spironolactone (N = 9) |
|---|---|---|---|---|
| BW (g) | 31.95 ± 0.69 | 30.48 ± 0.52 | 29.63 ± 0.62 | 28.84 ± 0.91 |
| LV wwt (mg) | 140.06 ± 9.71[b] | 182.03 ± 8.45 | 142.69 ± 4.13[b] | 145.96 ± 9.27[b] |
| LV wwt/BW (mg/g) | 4.38 ± 0.29[b] | 5.99 ± 0.28 | 4.84 ± 0.18[b] | 5.07 ± 0.30 |
| MAP (mmHg) | 80.77 ± 2.54 | 99.03 ± 6.82 | 95.88 ± 5.03 | 103.99 ± 6.66 |
| heart rate (bpm) | 406.41 ± 15.83 | 403.23 ± 7.98 | 407.11 ± 10.37 | 410.78 ± 11.70 |
| EF (%) | 56.49 ± 2.13 | 51.14 ± 2.49 | 57.89 ± 1.80 | 58.59 ± 1.40 |
| LVESP (mmHg) | 92.92 ± 3.04 | 139.36 ± 8.79 | 129.95 ± 7.64 | 137.39 ± 6.77 |
| LVEDP (mmHg) | 7.31 ± 0.78[b] | 15.49 ± 1.95 | 8.32 ± 1.10[b] | 14.93 ± 1.30 |
| $\tau_w$ (ms) | 7.19 ± 0.33[b] | 8.73 ± 0.41 | 7.05 ± 0.25[b] | 7.52 ± 0.32 |

[a]Data are shown as mean values with standard error of the mean (SEM). The homogeneity of variances was tested using the Levene test. In the case of homogenous variances, one way ANOVA followed by a Dunnett's post hoc test versus the Ang II placebo group was performed. In the case of heterogeneous variances, one way ANOVA on rank-transformed values followed by Dunnett's post hoc test versus the ANG II placebo group was performed. [b]$p < 0.05$ was defined as significant. All analyses were performed using SAS (version 8.2) for SUN 4 via interface software EverStat, version 5.0. Abbreviations: BW, body weight; MAP, mean arterial pressure; LV, left ventricle; wwt, wet weight; EF, ejection fraction; LVESP, left ventricle end systolic pressure; LVEDP, left ventricle end diastolic pressure.
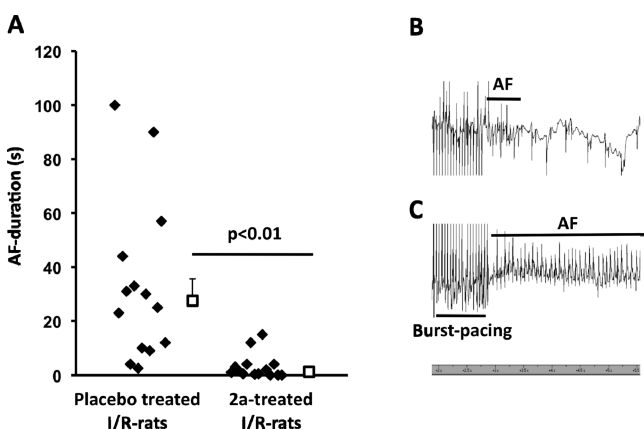


**Figure 8.** CatA inhibition reduces duration of atrial fibrillation (AF) induced by burst-pacing in rats with ischemia/reperfusion (I/R) ($n = 14$ per group). Individual AF duration is shown in black diamonds. Median AF duration is shown in white squares (A). Representative atrial electrograms during electrophysiological measurements in **2a**-treated I/R rats (B) and in placebo treated I/R rats (C). Statistical analysis was done by ANOVA. Significance was set to $p < 0.05$.

lead for our CatA inhibitor program. Rational design using X-ray crystallographical data guided the following lead optimization strategy, which was successful in overcoming the cell permeability issue associated with **8a** and delivered CatA inhibitors with high nanomolar in vitro activity and oral bioavailability. Pharmacological studies undertaken with **2a**, **15a**, **15b** confirmed the reported influence of CatA inhibition on renal bradykinin levels and resulted in the identification of beneficial effects in models of cardiac hypertrophy and of atrial fibrillation after administration of **2a**. On the basis of more detailed pharmacological investigations, which will be reported elsewhere, we were able to select one of our novel CatA inhibitors as a drug candidate, which is currently in phase I clinical trials.

### ■ EXPERIMENTAL SECTION

All commercially available reagents and solvents were used without further purification. Reversed phase high pressure chromatography was conducted on an Abimed Gilson instrument using a LiChrospher 100 RP-18e (5 μm) column from Merck. Nuclear magnetic resonance ($^1$H NMR) spectra were recorded in DMSO-$d_6$ on a Bruker Avance DRX 500, an Avance II 400, or Avance III 600 at room temperature. Chemical shifts are reported in as δ values from an internal tetramethylsilane

standard. Purity and characterization of compounds were established by a combination of LCMS and NMR analytical techniques. The purity of the final compound is >95% unless otherwise noted. The employed HPLC and LCMS methods (columns, eluents, gradients, and flow rates) are described below and are specified for each described compound. The HPLC−MS instrumentation was used with one of the two following setups: (A) Waters Aquity UPLC system equipped with a Waters Aquity autosampler, UPLC pump, and a diode array and the HPLC eluent coupled with a 1:3 split to a Waters Aquity SQD single quadrupole mass spectrometer with electrospray ionization, with spectra scanned from 100 to 1300 amu in positive and negative modes (LC3, LC5, LC6, LC7); (B) Agilent series 1100 system equipped with a degasser G1322A, bin pump G1312A, ALS G1313A, col comp G1316A, DAD G1315A, and MSD G1946A, with the HPLC eluent coupled to a mass spectrometer with electrospray ionization and with spectra scanned from 110 to 1000 amu in positive and negative modes (LC1, LC2, LC4).

**LC1.** Column: YMC-Pack Jsphere H80, 33 mm × 2.1 mm, 4 μm. Flow: 1.3 mL/min. Room temperature. Eluent A: water + 0.05 % TFA. Eluent B: ACN + 0.05% TFA. Gradient: from 95% A + 5% B to 5% A + 95% B within 2.5 min. MS ionization method: ES$^+$.

**LC2.** Column: YMC-Pack Jsphere H80, 33 mm × 2.1 mm, 4 μm. Flow: 1.0 mL/min. Room temperature. Eluent A: water + 0.05% TFA. Eluent B: ACN + 0.05% TFA. Gradient: 98% A + 2% B for 1.0 min, then to 5% A + 95% B within 4.0 min, then 5% A + 95% B for 1.25 min. MS ionization method: ES$^+$.

**LC3.** Column: Waters XBridge C18, 50 mm × 4.6 mm, 2.5 μm. Flow: 1.7 mL/min. 40 °C. Eluent A: water + 0.05% TFA. Eluent B: ACN + 0.05% TFA. Gradient: 95% A + 5% B for 0.3 min, then to 5% A + 95% B within 3.2 min, then 5% A + 95% B for 0.5 min. MS ionization method: ES$^+$.

**LC4.** Column: Merck Chromolith FastGrad RP-18e, 50 mm × 2 mm. Flow: 2.0 mL/min. Room temperature. Eluent A: water + 0.05% TFA. Eluent B: ACN + 0.05% TFA. Gradient: 98% A + 2% B for 0.2 min, then to 2% A + 98% B within 2.2 min, then 2% A + 98% B for 0.8 min, then to 98% A + 2% B within 0.1 min, then 98% A + 2% B for 0.7 min. MS ionization method: ES$^+$.

**LC5.** Column: Waters XBridge C18, 50 mm × 4.6, 2.5 μm. Flow: 1.3 mL/min. Room temperature. Eluent A: water + 0.1% FA. Eluent B: ACN + 0.08% FA. Gradient: from 97% A + 3% B to 2% A + 98% B within 18.0 min, then 2% A + 98% B for 1.0 min, then to 97% A + 3% B within 0.5 min, then 97% A + 3% B for 0.5 min. MS ionization method: ES$^+$.

**LC6.** Column: Waters XBridge C18, 50 mm × 4.6 mm, 2.5 μm. Flow: 1.7 mL/min. 50 °C. Eluent A: water + 0.05% TFA. Eluent B: ACN + 0.05% TFA. Gradient: 95% A + 5% B for 0.2 min, then to 5% A + 95% B within 2.2 min, then 5% A + 95% B for 1.1 min, then to 95% A + 5% B within 0.1 min, then 95% A + 5% B for 0.9 min. MS ionization method: ES$^+$.

**LC7.** Column: Waters XBridge C18, 50 mm × 4.6 mm, 2.5 μm. Flow: 1.7 mL/min. 40 °C. Eluent A: water + 0.05% TFA. Eluent B: ACN + 0.05% TFA. Gradient: from 95% A + 5% B to 5% A + 95% B within 3.3 min, then 5% A + 95% B for 0.55 min, then to 95% A + 5% B within 0.15 min. MS ionization method: ES⁺.

**(S)-3-{[1-(2-Fluorophenyl)-5-hydroxy-1H-pyrazole-3-carbonyl]amino}-3-o-tolylpropionic Acid (8a). General Procedure A for the Synthesis of Compounds 8.** *Step 1.* Sulfuric acid (400 mL) was added slowly to water (400 mL). After the mixture was cooled to 5 °C, 2-fluorophenylhydrazine hydrochloride (123 g, 757 mmol) was added resulting in a brown suspension. Then a solution of oxalacetic acid (100 g, 757 mmol) in water (400 mL) was added slowly during a period of 25 min. After 2 h the conversion was complete and the solid was filtered. After a wash with water, the solid was dried. The product 1-(2-fluorophenyl)-5-hydroxy-1H-pyrazole-3-carboxylic acid 7a was obtained as light brown solid (151 g, 90%) and used directly in the next step.

*Step 2.* An amount of 0.45 mmol of 1-(2-fluorophenyl)-5-hydroxy-1H-pyrazole-3-carboxylic acid was dissolved in 5 mL of DMF, and 0.54 mmol of TOTU and 1.125 mmol of NEM were added. The mixture was stirred for 5 min at room temperature. Then 0.495 mmol of (S)-3-amino-3-o-tolylpropionic acid was added and the mixture stirred overnight at room temperature. The solvent was evaporated in vacuo and the residue subjected to preparative HPLC to give **8a** in a yield of 28%. ¹H NMR (500 MHz, DMSO) δ 8.60 (d, 1H), 7.55 (m, 2H), 7.45 (m, 2H), 7.35 (m, 1H), 7.15 (m, 3H), 5.80 (s, 1H), 5.60 (q, 1H), 2.90 (dd, 2H), 2.70 (dd, 2H), 2,40 (s, 3H). LCMS (LC3): *m/z* 383,13 (M + H).

**General Procedure B for the Synthesis of Compounds 2 and 13−16 (Steps 1−4). (S)-3-{[1-(2-Fluorophenyl)-5-((R)-2-hydroxy-3,3-dimethylbutoxy)-1H-pyrazole-3-carbonyl]amino}-3-o-tolylpropionic Acid (15a).** *Step 1.* Dimethyl acetylenedicarboxylate (87.4 g, 757 mmol) was added to a solution of 2-fluorophenylhydrazine hydrochloride (100 g, 615 mmol) in methanol (1 L) at 0 °C. Then triethylamine (125 g, 1.23 mol) was added slowly during 60 min. The solution was stirred for 16 h at room temperature. The solvent was then removed under reduced pressure and the residue dissolved in EA (500 mL). After washing with aqueous hydrochloric acid (500 mL), the solvent was removed under reduced pressure and methyl 1-(2-fluorophenyl)-5-hydroxy-1H-pyrazole-3-carboxylate **11a** was obtained as an off white solid in quantitative yield.

*Step 2.* An amount of 200 mg (0.85 mmol) of methyl 1-(2-fluorophenyl)-5-hydroxy-1H-pyrazole-3-carboxylate **11a** was dissolved in 5 mL of DMF. Then 552 mg (1.7 mmol) of cesium carbonate and 152 mg (0.85 mmol) of 1-bromo-3,3-dimethylbutan-2-one were added, and the mixture was heated to 50 °C for 6 h. Then the mixture was filtered and the solvent removed in vacuo. The obtained crude title compound 5-(3,3-dimethyl-2-oxo-butoxy)-1-(2-fluorophenyl)-1H-pyrazole-3-carboxylic acid methyl ester was subjected to hydrolysis without further purification.

*Step 3.* An amount of 100 mg (0.3 mmol) of 5-(3,3-dimethyl-2-oxobutoxy)-1-(2-fluorophenyl)-1H-pyrazole-3-carboxylic acid methyl ester was dissolved in 5 mL of MeOH. Then 0.7 mmol of lithium hydroxide and 2 mL of water were added, and the mixture was stirred overnight at room temperature. The solvent was removed in vacuo and the residue subjected to aqueous workup with a 10% solution of citric acid and DCM. The organic phase was dried and the solvent removed in vacuo to give 5-(3,3-dimethyl-2-oxobutoxy)-1-(2-fluorophenyl)-1H-pyrazole-3-carboxylic acid, which was used without further purification in the next step.

*Step 4.* An amount of 324 mg (0.675 mmol) of 5-(3,3-dimethyl-2-oxobutoxy)-1-(2-fluorophenyl)-1H-pyrazole-3-carboxylic acid was dissolved in 5 mL of DMF, and 0.675 mmol of TOTU and 1.35 mmol of EDIA were added. The mixture was stirred for 5 min at room temperature. Then 0.675 mmol of (S)-3-amino-3-(2-methylphenyl)-propionic acid was added, and the mixture was stirred overnight at room temperature. After evaporation of the solvent, the residue was subjected to preparative HPLC to give (S)-3-{[5-(3,3-dimethyl-2-oxobutoxy)-1-(2-fluorophenyl)-1H-pyrazole-3-carbonyl]amino}-3-o-tolylpropionic acid (**13a**) in a yield of 67%. ¹H NMR (400 MHz, DMSO) δ 8.70 (d,

1H), 7.65 (m, 1H), 7.60 (m, 1H), 7.50 (m, 2H), 7.40 (m, 1H), 7.10 (m, 3H), 6.10 (s, 1H), 5.60 (q, 1H), 5.25 (s, 2H), 2.90 (dd, 1H), 2.70 (dd, 1H), 2.40 (s, 3H), 1.10 (s, 9H) LCMS (LC4): *m/z* 482,18 (M + H).

*Step 5.* An amount of 50 mg (0.1 mmol) of (S)-3-{[5-(3,3-dimethyl-2-oxobutoxy)-1-(2-fluorophenyl)-1H-pyrazole-3-carbonyl]amino}-3-o-tolylpropionic acid **13a** was dissolved in 5 mL of methanol, and 0.05 mmol of sodium borohydride was added. The mixture was stirred at room temperature overnight. The solvent was removed in vacuo and the residue subjected to preparative HPLC to give 52% of (S)-3-{[1-(2-fluorophenyl)-5-(2-hydroxy-3,3-dimethylbutoxy)-1H-pyrazole-3-carbonyl]amino}-3-o-tolylpropionic acid **14a**. An amount of 100 mg **14a** was separated into the two diastereomeric title compounds by HPLC on a chiral column (Chiralpak AD-H/55, 250 mm × 4.6 mm) at 30 °C (eluent, heptane/ethanol/MOH (15:1:1) + 0.1% TFA; flow, 1.0 mL/min). Then 45 mg of the first diastereomer (retention time, 16.35 min) eluted from the column and 40 mg of the second diastereomer (retention time, 21.15 min) eluted from the column were obtained, one of them being the diastereomer with *R* configuration in the alcohol moiety and the other being the diastereomer with *S* configuration in the alcohol moiety. The stereochemistry in the alcohol moiety was not determined; it was arbitrarily assigned *R* configuration in the first diastereomer eluted from the column **15a** and *S* configuration in the second diastereomer eluted from the column **16a**.

**(S)-3-{[1-(2-Fluorophenyl)-5-((R)-2-hydroxy-3,3-dimethylbutoxy)-1H-pyrazole-3-carbonyl]amino}-3-o-tolylpropionic Acid (15a).** ¹H NMR (500 MHz, DMSO) δ 8.65 (d, 1H), 7.60 (m, 2H), 7.60 (m, 1H), 7.45 (m, 2H), 7.35 (m, 1H), 7.10 (m, 3H), 6.20 (s, 1H), 5.60 (q, 1H), 4.90 (d, 1H), 4.25 (dd, 1H), 3.95 (dd, 1H), 2.90 (dd, 1H), 2.70 (dd, 1H), 2.45 (s, 3H), 0.85 (s, 9H). LCMS (LC5): *m/z* 484.34 (M + H), *t*R = 10.16 min.

**(S)-3-{[1-(2-Fluorophenyl)-5-((S)-2-hydroxy-3,3-dimethylbutoxy)-1H-pyrazole-3-carbonyl]amino}-3-o-tolylpropionic Acid (16a).** ¹H NMR (500 MHz, DMSO) δ 8.65 (d, 1H), 7.6 (m, 2H), 7.45 (m, 2H), 7.35 (m, 1H), 7.10 (m, 3H), 6.20 (s, 1H), 5.60 (q 1H), 4.90 (bs, 1H), 4.20 (dd, 1H), 3.95 (dd, 1H), 2.90 (dd, 1H), 2.70 (dd, 1H), 2.45 (s, 3H), 0.85 (s, 9H). LCMS (LC5): *m/z* 484.34 (M + H), *t*R = 10.33 min.

**(S)-3-(2,4-Dichlorophenyl)-3-{[5-(3,3-dimethyl-2-oxobutoxy)-1-(2-fluorophenyl)-1H-pyrazole-3-carbonyl]amino}-propionic Acid (13b).** Following general procedure B and using (S)-3-amino-3-(2,4-dichlorophenyl)propionic acid in step 4 gave **13b**. ¹H NMR (500 MHz, DMSO) δ 8.90 (d, 1H), 7.7 (m, 3H), 7,55 (m, 3H), 7.5 (m, 1H), 7.4 (m, 2H), 6.20 (s, 1H), 5.70 (q 1H), 5.30 (s, 2H), 2.90 (dd, 1H), 2.65 (dd, 1H), 1.10 (s, 9H). LCMS (LC4): *m/z* 536.20 (M + H).

**(S)-3-(2,4-Dichlorophenyl)-3-{[1-(2-fluorophenyl)-5-((R)-2-hydroxy-3,3-dimethylbutoxy)-1H-pyrazole-3-carbonyl]amino}-propionic Acid (15b).** Following general procedure B and using (S)-3-amino-3-(2,4-dichlorophenyl)propionic acid in step 4 gave **15b**. ¹H NMR (500 MHz, DMSO) δ 8.90 (d, 1H), 7.60 (m, 4H), 7.45 (m, 2H), 7.40 (m, 1H), 6.25 (s, 1H), 5.70 (q, 1H), 4.90 (d, 1H), 4.25 (dd, 1H), 3.95 (dd, 1H), 2.90 (dd, 1H), 2.65 (dd, 1H), 0.85 (s, 9H). LCMS (LC5): *m/z* 538.24 (M + H), *t*R = 11.13 min.

**(S)-3-(2,4-Dichlorophenyl)-3-{[1-(2-fluorophenyl)-5-((S)-2-hydroxy-3,3-dimethylbutoxy)-1H-pyrazole-3-carbonyl]amino}-propionic Acid (16b).** Following general procedure B and using (S)-3-amino-3-(2,4-dichlorophenyl)propionic acid in step 4 gave **16b**. ¹H NMR (500 MHz, DMSO) δ 8.85 (d, 1H), 7.60 (bm, 4H), 7.45 (m, 2H), 7.40 (m, 1H), 6.25 (s, 1H), 5.70 (q, 1H), 4.90 (bs, 1H), 4.25 (dd, 1H), 3.95 (dd, 1H), 2.90 (dd, 1H), 2.65 (dd, 1H), 0.85 (s, 9H). LCMS (LC5): *m/z* 538,24 (M + H), *t*R = 11.36 min.

**(S)-3-{[1-(2-Fluorophenyl)-5-methoxy-1H-pyrazole-3-carbonyl]amino}-3-(2-methylphenyl)propionic Acid (2a).** Following steps 1−4 from general procedure B using MeI in step 2 gave **2a**. ¹H NMR (500 MHz, DMSO) δ 8.70 (d, 1H), 7.60 (m, 2H), 7,45 (m, 2H), 7.35 (m, 1H), 7.15 (m, 3H), 6.20 (s, 1H), 5.60 (q, 1H), 3.90 (s, 3H), 2.90 (dd, 1H), 2.70 (dd, 1H), 2.45 (s, 3H). LCMS (LC3): *m/z* 398,18 (M + H).

**Expression and Purification of Recombinant Human Procathepsin A.** ORF coding for human procathepsin A (proCatA, Ala29-Tyr480, BC000597) was cloned from full-length cDNA in frame with

insect prepromelitin signal sequence and Myc-tag followed by a 10xHis at the C-terminal end of the coding protein. The DNA was ligated into the multiple cloning site of the baculovirus transfer vector[25] pVL1393 vector (AB vector). After co-transfection of plasmids with baculovirus-DNA (FlashBac GOLD, Oxford Expression Technologies),[26] the virus was amplified in two steps in *Spodoptera frugiperda*[27] cell line SF9 in SF900II medium (Invitrogen) supplemented with 5% FCS. Recombinant virus was harvested 5 days post-transfection. The virus titers were determined by plaque assay method[28] and reached about $1 \times 10^8$ pfu/mL.

ProCatA was expressed for 72 h dpi at MOI 3 in $1.1 \times 10^6$ cells/mL High Five cells growing in ExCell405 medium at a 4 L scale using four vented 3000 mL flasks (Corning) at 110 rpm at 27 °C.

Purification steps were carried out at 4 °C using a ÄKTA explorer system (GE) for chromatography. His-tagged protein was bound directly to metal chelate ligand[29] from the clarified insect cell supernatant using a 5 mL HisTrap column HP (GE) with a flow rate of 3 mL/min. After a wash with 10 CV, 20 mM $NaPO_4$, pH 8.0, 500 mM NaCl within a linear gradient, bound protein was eluted from 0% to 100% buffer, 20 mM $NaPO_4$, pH 8.0, 500 mM NaCl, and 1000 mM imidazole. Fractions were collected and analyzed on SDS–PAGE,[30] and fractions containing proCatA were pooled. Protein was polished by size exclusion chromatography (SEC) on Superdex 26/60 200 HR (GE) using 300 mM NaCl, 50 mM Tris-HCl, pH 7.5, as buffer.

**Cathepsin A Activity Assays.** Recombinant human proCatA was proteolytically activated with recombinant human cathepsin L (R&D Systems, no. 952-CY) according to the manufacturer's instructions. Briefly, proCatA was incubated at 10 μg/mL with cathepsin L (CatL) at 1 μg/mL in 25 mM 2-(N-morpholino)ethanesulfonic acid (MES), 5 mM dithiothreitol (DTT), pH 6.0, for 15 min at 37 °C. CatL activity was then stopped by the addition of 10 μM N-(trans-epoxysuccinyl)-L-leucine-4-guanidinobutylamide (E64, Sigma). The activated CatA was diluted in 25 mM MES, 5 mM DTT, pH 5.5, to a final concentration of 833 ng/mL and mixed with compounds or vehicle in a multiple assay plate. After incubation for 15 min at room temperature a bradykinin peptide carrying a N-terminal BodipyFL label (Jerini Peptide Technology) was added to the assay mixture to a final concentration of 2 μM. After incubation for 15 min at room temperature the reaction was stopped by the addition of 130 mM 2-(4-(2-hydroxyethyl)-1-piperazinyl)ethansulfonic acid, pH 7.4, containing 0.013% Triton X-100, 0.13% coating reagent (Caliper Life Sciences), 6.5% DMSO, and 20 μM ebelactone B (Sigma, no. E0886). Uncleaved substrate and product were then separated by a microfluidic capillary electrophoresis on a LabChip 3000 drug discovery system (12-Sipper-Chip, Caliper Life Sciences) and quantified by determination of the respective peak areas. Substrate turnover was calculated by dividing product peak area by the sum of substrate and product peak areas. The enzyme activity and the inhibitory effect of any test compound could thus be quantified. The efficacy of test compounds is expressed as the concentration that induces 50% inhibition of enzyme activity ($IC_{50}$).

**Biochemical Selectivity Assays.** CatA inhibitor selectivity was determined against several proteases. Recombinant human cathepsin L (CathL, R&D Systems, no. 952-CY), cathepsin S (CathS, R&D Systems, no. 1183-CY), ACE (R&D Systems, no. 929-ZN), ACE2 (R&D Systems, no. 933-ZN), DPPIV (R&D Systems, no. 1180-SE), NEP (R&D Systems, no. 1182-ZNC), Kallikrein (R&D Systems, no. 2337-SE), human cathepsin D from liver (CathD, Enzo Life Sciences, no. BML-SE199), human chymotrypsin from pancreatic tissue (US Biological, no. C5070-08), factor Xa from human plasma (Xa, US Biological, no. F0018-15), and recombinant HCV NS3/4a (AnaSpec, no. 61017-10) were tested accoding to manufacturers' instructions (adapted to 384-well format). Briefly, enzymes (3 μL) and inhibitor (3 μL), diluted in appropriate reaction buffer, were transferred into black 384-well low volume plates (medium binding) and were incubated for 15 min at room temperature followed by the addition of substrate solution (diluted in reaction buffer: CathL (ES008, R&D), CathS (ES002, R&D), CathD (M-1895, Bachem), ACE (ES005, R&D), ACE2 (ES007, R&D), DPPIV (L-1225, Bachem), NEP (ES005, R&D), Kalikrein (P9273, Sigma), chymotrypsin (J-1355, Bachem), Xa (ES008, R&D), NS3/4a (61017-10, AnaSpec)) to a final volume of 9 μL. After

20−30 min of incubation at room temperature fluorescence intensity was measured in a Tecan Safire2 plate reader (various emission/excitation wavelengths based on use substarte). The % inhibition and $IC_{50}$ values were calculated based on internal high and low controls.

**Crystallography.** To obtain the active form of the enzyme, the 54 kDa CatA precursor was proteolytically transformed into the active mature form by cleavage of a 2 kDa excision peptide with trypsin-Sepharose followed by gel filtration.

CatA was crystallized using the hanging drop method. Then 1 μL of protein solution, containing 6.5 mg/mL cathepsin A, 25 mM Tris-HCl (pH 8.0), and 300 mM NaCl, was mixed with 1 μL of reservoir solution, containing 100 mM sodium acetate (pH 4.5), 18−20% PEG400, and 100 mM $CdCl_2$, and set to equilibrate at 4 °C. Rod-shaped crystals appeared in about 1 week. Crystals were soaked with inhibitors by transferring them to a drop of 9 μL reservoir solution with 1 μL of a 100 mM solution of **8a** or **15a** in DMSO. For cryoprotection, 20% glycerol was added to the soaking solution and the crystal was picked with a small nylon loop and flash frozen in liquid nitrogen. Data were measured at the ESRF at beamlines ID29 and ID14-4 and processed with XDS/XSCALE[31] as implemented in APRV.[32] The structures were solved using a previously solved cathepsin A structure as a starting model. The initial model was obtained by molecular replacement with Phaser[33] using the CatA precursor structure[14] (PDB code 1IVY) as a starting model. Model building was done with Coot,[34] and refinement was done with Buster.[35]

**Molecular Modeling and Visualization.** Docking was performed with GLIDE 3.5 in standard precision mode without further minimization, using Glidescore for ranking. All ligands were prepared using LigPrep including the Epik approach.[36] All protomers and tautomers existing at pH 7.4 were included in the docking studies. The docking results were filtered manually. All graphics were generated using Sybyl 8.0[37]

**In Vivo Experiments.** All experiments using animals were performed in accordance with the German law for the protection of animals and adhered to the international animal welfare legislation and rules.

**Pharmacokinetic Studies.** Pharmacokinetic parameters of **2a**, **15a**, and **15b** were determined in male Sprague−Dawley rats (Harlan Winkelmann, Germany). After single oral administration of 10 mg/kg in a solution consisting of glycofurol 75 (19%), Cremophor RH40 (6%), and water (75%), plasma and tissue samples were taken at eight time points over 24 h. Three animals per time point were used in a nonserial sampling design. Heart tissue was homogenized with water (2 g of water for 1 g tissue) using a ball mill (Retsch). The respective compound concentrations in plasma and tissue homogenates were determined using an exploratory LCMS/MS method using a structurally related compound as internal standard. The area under the plasma concentration−time curve was calculated using the software WinNonlin (Pharsight Corporation).

**Pharmacological Studies.** For the diuresis experiments male Wistar rats were anesthetized with urethane (1.25 mg/kg im) and the carotid artery and the jugular vein were cannulated for blood pressure control and for infusion with albumine in physiologic saline (0.28 mg $kg^{-1}$ $h^{-1}$) and bolus injection of compound. Animals were placed on a heating water pad. Infusion with albumin started directly after cannulation. After median lapratomy both ureters were cannulated with tubes and urine was sampled. Rats received iv bolus injections of compounds in 0.15% $Na_2CO_3$ 20 min after start of albumin infusion. Urine was collected in five succeeding time periods of 20 min. The volume of each urine sample was measured.

Cardiac hypertrophy was induced in male B6.129P2-ApoE/J mice (ApoE ko mice) by continuous 28 days of infusion of Ang II (1 μg $kg^{-1}$ $min^{-1}$ sc) via osmotic mini pumps (model 2004, ALZET Osmotic Pumps, Durect Corporation, U.S.). Before subcutaneous implantation minipumps were filled with either sterile saline (NaCl placebo group) or Ang II diluted in sterile saline (all other groups). The minipumps were subcutaneously implanted under short isoflurane anesthesia and were thereafter active for the next 4 weeks. Oral treatment started on the day of surgery approximately 2 h after recovery from surgery. **2a** was administered at 100 mg $kg^{-1}$ $day^{-1}$ in HEC 0.6% + Tween 0.5%

(vehicle) by oral gavage, while within the Ang II placebo group and the NaCl placebo control group animals received vehicle only. As a reference compound spironolactone at a dose of 100 mg/kg po twice daily was chosen.

After 28 days, the final functional examinations by aortic arch tip catheter analysis and left ventricular pressure–volume (p–v) loop measurements were performed using a 1.4 French catheter (SPR-839, Millar Instruments, U.S.). Briefly, the animals were anesthetized with thiopental at 100 mg/kg ip. As a next step the right carotid artery was prepared for catheter insertion and the p–v loop catheter was initially placed within the ascending aortic arch for MAP and HR registration and finally placed within the left ventricular chamber for steady-state characterization of p–v loop parameters. Afterward the abdomen was opened below the diaphragm and the vena cava was exposed for ligation. Using complete occlusion of the inferior vena cava the preload-recruitable left ventricular performance was registered. All parameters were digitally recorded using the Notocord hem evolution software, and the analysis of the different functional parameters was performed offline at a later time point.

Atrial arrhythmogenic substrate was induced by ventricular ischemia reperfusion (I/R). In 28 male Wistar rats (3–4 months old) a left-sided thoracotomy was performed and myocardial ischemia was induced by temporary occlusion of the left coronary artery close to its origin from the aorta for 30 min. Ischemia induction was followed by reperfusion. CatA inhibitor **2a** (30 mg kg$^{-1}$ day$^{-1}$) was administered via oral lavage once a day in 14 I/R rats. Fourteen placebo treated I/R rats received vehicle only (HEC 0.6% + Tween 0.5%). After 3 months of treatment, all rats were anesthetized (intraperitoneal injection of pentobarbital) and electrophysiological measurements were performed in open chest experiments. Atrial pacing threshold was determined and unipolar pacing was performed from the surface of the left atrial appendage using a pacing electrode (tip electrode) next to a custom-made multiple action potential catheter (Franz-like electrode) with a pulse of 1 ms and at twice the diastolic threshold. The longest episode of atrial fibrillation induced by five repetitive 1 s bursts of stimuli (very rapid pacing, cycle length of 10 ms) was determined. When atrial electrograms showed a rapid atrial rate, cycle length of <70 ms, and duration of >5 beats, atrial fibrillation was diagnosed.

**Urinary Bradykinin.** Bradykinin in urine was determined from male Wistar rats collected over a period of 6 h before and after treatment of rats with compounds **2a** and **15a,b** at 30 mg kg$^{-1}$ day$^{-1}$. A commercially available RIA (Bachem) was used according to the manufacturer's instructions.

## ASSOCIATED CONTENT

**S** **Supporting Information**
Experimental and spectoscopic data for nonkey compounds and X-ray crystallographic data. This material is available free of charge via the Internet at http://pubs.acs.org.

## AUTHOR INFORMATION

**Corresponding Author**
*Phone: +49 69 305 12982. E-mail: sven.ruf@sanofi.com.

**Present Address**
§Evangelisches Krankenhaus, Oberhausen, Germany.

**Notes**
The authors declare no competing financial interest.

## ACKNOWLEDGMENTS

## ABBREVIATONS USED

CatA, cathepsin A; ANG II, angiotensin II; EA, ethyl acetate; EDIA, ethyldiisoproylamine; EF, ejection fraction; MAP, mean arterial pressure; NEP, neprylisine; HPLC, high pressure liquid chromatography; HR, heart rate; LV, left ventricle; LVEDP, left ventricular end diastolic pressure; LVESP, left ventricular end systolic pressure; RIA, radioactive immunoassay; NEM, N-ethylmorpholine; RP, reverse phase; TOTU, O-((ethoxycarbonyl)cyanomethyleneamino)-N,N,N′,N′-tetramethyluronium tetrafluoroborate; wwt, wet weight

## REFERENCES

(1) Hiraiwa, M. Cathepsin A/protective protein: an unusual lysosomal multifunctional protein. *Cell. Mol. Life Sci.* **1999**, 55, 894–907.

(2) (a) Itoh, K.; Takiyama, N.; Kase, R.; Kondoh, K.; Sanao, A.; Oshima, A.; et al. Purification and characterization of human lysosomal protective protein expressed in stably transformed Chinese hamster ovary cells. *J. Biol. Chem.* **1993**, 268, 1180–1186. (b) Jackman, H. J.; Tan, F.; Tamei, H.; Beurling-Harbury, C.; Li, X.-Y.; Skidgel, R. A.; et al. A deamidase in human platelets that deamidates tachykinins: probable identity with the lysosomal protective protein. *J. Biol. Chem.* **1990**, 265, 11265–11272. (c) Jackman, H. J.; Morris, P. W.; Deddish, P. A.; Skidgel, R. A.; Erdös, E. G. Inactivation of endothelin I by deamidase (lysosomal protective protein). *J. Biol. Chem.* **1992**, 267, 2872–2875. (d) Itoh, K.; Kase, R.; Simmoto, M.; Satake, A.; Sakaruba, H.; Suzuki, Y. Protective protein as an endogenous endothelin degradation enzyme in human tissues. *J. Biol. Chem.* **1995**, 270, 515–518.

(3) (a) d'Azzo, A.; Hoogeveen, A. T.; Reuser, J. J.; Robinson, H.; Galjaard, H. Molecular defect in combined β-galactosidase and neuraminidase deficiency in man. *Proc. Natl. Acad. Sci. U.S.A.* **1982**, 79, 4535–4539. (b) Zhou, X. Y.; Morreau, H.; Rottier, R.; Davis, D.; Bonten, E.; Gillemans, N.; et al. Mouse model for the lysosomal disorder galactosialidosis and correction of the phenotype with overexpressing erythroid precursor cells. *Genes Dev.* **1995**, 9, 2623–2634.

(4) Seyrantepe, V.; Hinek, A.; Junzheng, P.; Fedjaev, M.; Sheila, E.; Yoshito, K.; Canuel, M.; Itoh, K.; Morales, C. R.; Lavoie, J.; Tremblay, J.; Pshezhetsky, A. V. Enzymatic activity of lysosomal carboxypeptidase (cathepsin) A is required for proper elastic fiber formation an inactivation of endothelin-1. *Circulation* **2008**, 117, 1973–1981.

(5) Miller, J. J.; Changaris, D. G.; Levy, R. S. Conversion of angiotensin I to angiotensin II by cathepsin A isozymes of porcine kidney. *Biochem. Biophys. Res. Commun.* **1988**, 154, 1122–1129.

(6) Ito, H.; Majima, M.; Nakajima, S.-i.; Hayashi, I.; Katori, M.; Izumi, T. Effect of prolonged administration of a urinary kininase inhibitor ebelactone B on the development of deoxycorticosterone acetate-salt hypertension in rats. *Br. J. Pharmacol.* **1999**, 126, 613–620.

(7) Hayashi, I.; Majima, M.; Fujita, T.; Okumura, T.; Kumagai, Y.; Tomita, N.; et al. In vivo transfer of antisense oligonucleotide against urinary kininase blunts deoxycorticosterone acetate-salt hypertension in rats. *Br. J. Pharmacol.* **2000**, 131, 820–826.

(8) Cuervo, A. M.; Mann, L.; Bonten, E. J.; d'Azzo, A.; Dice, J. F. Cathepsin A regulates chaperone-mediated autophagy through cleavage of the lysosomal receptor. *EMBO J.* **2003**, 22, 47–59.

(9) Westermann., D.; Schultheiss, H. P.; Tschöpe, C. New perspective on the tissue kallikrein-kinin system in myocardial infarction: role of angiogenesis and cardiac regeneration. *Int. Immunopharmacol* **2008**, 8, 148–154.

(10) Kam, J.-D. Dual ACE/NEP inhibitors—more than playing the ACE card. *J. Hum. Hypertens.* **2006**, 20, 478–481.

(11) Weiner, B.; Szymanski, W.; Jansen, D. B.; Minnard, A. J.; Ferninga, B. L. Recent advances in the catalytic asymmetric synthesis of β-amino acids. *Chem. Soc. Rev.* **2010**, 39, 1656–1691.

(12) Montalbetti, C. A. G. N.; Falque, V. Amide bond formation and peptide coupling. *Tetrahedron* **2005**, 61, 10827–10852.

(13) Oprea, T. I.; Davis, M.; Teague, S. J.; Leeson, P. D. Is there a difference between leads and drugs? A historical perspective. *J. Chem. Inf. Comput. Sci.* **2001**, *41*, 1308−1315.

(14) Artursson, P. Epithelial transport of drug in cell culture: a model for studying the passive diffusion of drugs over intestinal absorbtive (Caco-2) cells. *J. Pharm. Sci.* **1990**, *79*, 476−482.

(15) Protein Data Bank deposition codes for **8a** and **15a**: 4az0 and 4az3.

(16) Rudenko, G.; Bonten, E.; d'Azzo, A.; Hol, W. G. J. Three-dimensional structure of the human protective protein: structure of the precursor form suggests a complex activation mechanism. *Structure* **1995**, *3*, 1249−1259.

(17) Rudenko, G.; Bonten, E.; d'Azzo, A.; Hol, W. G. J. Structure determination of the human protective protein: twofold averaging reveals the three-dimensional structure of a domain, which was entirely absent in the initial model. *Acta Crystallogr.* **1996**, *D52*, 923−936.

(18) Stella, V. J.; Himmelstein, J. Prodrugs and site-specific drug delivery. *J. Med. Chem.* **1980**, *23*, 1275−1282.

(19) Verdonk, M. L.; Cole, J. C.; Taylor, R. SuperStar: a knowledge-based approach for identifying interaction sites in proteins. *J. Mol. Biol.* **1999**, *289* (4), 1093−108.

(20) Friesner, R. A.; Banks, J. L.; Murphy, R. B.; Halgren, T. A.; Klicic, J. J.; Mainz, D. T.; Repasky, M. P.; Knoll, E. H.; Shelley, M.; Perry, J. K.; Shaw, D. E.; Francis, P.; Shenkin, P. S. Glide: a new approach for rapid, accurate docking and scoring. 1. Method and assessment of docking accuracy. *J. Med. Chem.* **2004**, *47*, 1739.

(21) See www.cerep.fr for more details.

(22) Katori, M.; Majima, M. The renal kallikrein−kinin system: its role as a safety valve for excess sodium intake, and its attenuation as a possible etiologic factor in salt-sensitive hypertension. *Crit. Rev. Clin. Lab. Sci.* **2003**, *40*, 43−115.

(23) Linz, W.; Schoelkens, B. A. A specific B2-bradykinin receptor antagonist HOE 140 abolishes the antihypertrophic effect of ramipril. *Br. J. Pharmacol.* **1992**, *105*, 771−772.

(24) Jackman, H. L.; Massad, M. G.; Sekosan, M.; Tan, F.; Brovkovych, V.; Marcic, B. M.; Erdös, E. G. Angiotensin 1-9 and 1-7 release in human heart. Role of cathepsin A. *Hypertension* **2002**, *39*, 976−981.

(25) Kitts, P. A.; Possee, R. D. A method for producing recombinant baculovirus expression vectors at high frequency. *BioTechniques* **1993**, *14*, 810−817.

(26) Patent applications EP1144666, WO0112829, and AU6460800.

(27) Vaughn, J. L.; Goodwin, R. H.; Tompkins, G. J.; McCawley, P. The establishment of two cell lines from the insect *Spodoptera frugiperda* (*Lepidoptera*; *Noctuidae*). *In Vitro* **1977**, *13*, 213−7.

(28) Brown, M; Faulkner, P. A plaque assay for nuclear polyhedrosis viruses using a solid overlay. *J. Gen. Virol.* **1977**, *36*, 361−364.

(29) Hochuli, E.; Bannwarth, W.; Döbeli, H.; Gentz, R.; Stüber, D. Genetic approach to facilitate purification of recombinant proteins with a novel metal chelate adsorbent. *Nat. Biotechnol.* **1988**, *6*, 1321−1325.

(30) Laemmli, U. K. Cleavage of structural proteins during assembly of the head of bacteriophage T4. *Nature* **1970**, *227*, 680−685.

(31) Kabsch, W. XDS. *Acta Crystallog.* **2010**, *D66*, 125−132.

(32) Kroemer, M.; Dreyer, M. K.; Wendt, K. U. APRV—a program for automated data processing, refinement and visualization. *Acta Crystallogr.* **2004**, *D60*, 1679−1682.

(33) McCoy, A. J.; Grosse-Kunstleve, R. W.; Adams, P. D.; Winn, M. D.; Storoni, L. D.; Read, R. J. Phaser crystallographic software. *J. Appl. Crystallog.* **2007**, *40*, 658−674.

(34) Emsley, P.; Cowtan, K. Coot: model-building tools for molecular graphics. *Acta Crystallog D* **2004**, *60*, 2126−2132.

(35) Bricogne, G.; Blanc, E.; Brandl, M.; Flensburg, C.; Keller, P.; Paciorek, W.; Roversi, P; Sharff, A.; Smart, O. S.; Vonrhein, C.; Womack, T. O. *BUSTER*; Global Phasing Ltd.: Cambridge, U.K., 2011.

(36) Shelley, J. C.; Choletti, A.; Frye, L. L.; Greenwood, J. R.; Timlin, M. R.; Uchimaya, M. Epik: a software program for pKa prediction and protonation state generation for drug-like molecules. *J. Comput.-Aided Mol. Des.* **2007**, *21*, 681−691.

(37) *Sybyl 8.0*; Tripos (1699 South Hanley Road, St. Louis, MO, U.S.).